An urban module coupled with the Variable Infiltration Capacity model to improve hydrothermal simulations in urban systems

Yibing Wang[1], Xianhong Xie[1*], Bowen Zhu[2], Arken Tursun[1], Fuxiao Jiang[3], Yao Liu[1], Dawei Peng[1], Buyun Zheng[1]

1. State Key Laboratory of Remote Sensing Science, Faculty of Geographical Science, Beijing Normal University, Beijing 100875, China
2. College of Water Science and Engineering, Taiyuan University of Technology, Taiyuan 030024, China
3. Institute of Earth Surface Dynamics, University of Lausanne, 1015 Lausanne, Switzerland

*Corresponding author:

Xianhong Xie (Beijing Normal University, xianhong@bnu.edu.cn)

16 **Abstract**

17   Global urban expansion has altered surface aerodynamics and hydrothermal dynamics, aggravating

18 environmental challenges such as urban heat/dry islands. To identify such environmental responses,

19 various physical models, including urban canyon models (UCMs) and land surface models (LSMs),

20 have been developed to represent surface hydrothermal processes. However, UCMs often treat a city as

21 a unified entity and overlook subcity heterogeneity. LSMs are generally designed for natural land covers

22 and lack the capability to capture urban characteristics. To address these limitations, the aim of this study

23 is to couple an urban module with a sophisticated LSM, i.e., the Variable Infiltration Capacity (VIC)

24 model. This coupled model, i.e., the VIC-urban model, is characterized by its ability to coordinate certain

25 critical urban features, including the urban geometry, radiative interactions, and human impacts.

26 Adopting Beijing as an evaluation site, the VIC-urban model shows higher performance than the original

27 version, with excellent accuracy in simulating sensible heat, latent heat, runoff, and land surface

28 temperature (LST). The absolute error is smaller than 25% for the sensible heat and latent heat, and

29 smaller than 12% and 30% for the LST and runoff, respectively, which indicates that VIC-urban can

30 effectively simulate hydrological and thermal fluxes in urban systems. Sensitivity analysis reveals that

31 the roof emissivity and interception capacity exert the greatest impact on the roof temperature and

32 evaporation, and the height-width ratio has the greatest influence on the canyon. Our work introduces a

33 reliable option for large-scale land surface simulations that accounts for urban environments, and is

34 among the first attempts to establish a systematic urban modelling framework of the VIC model. The

35 VIC-urban model enables the analysis of urbanization-induced environmental changes and

36 quantification of environmental variations among different urban configurations. The proposed model

37 can thus offer invaluable insights for urban planners and landscape designers.

38 **Key words:** Urban canyon models; VIC model; Hydrothermal processes; Urban system; Sensitivity

39 analysis

1. Introduction

Urban areas have been expanding globally and are characterized by increasing impervious surfaces and decreasing natural land coverage. This land cover change has led to alterations in surface aerodynamics and hydrothermal dynamics, resulting in decreased local evaporation and an exacerbation of temperature and extreme precipitation events (Yang et al., 2021). It has caused numerous environmental issues, such as urban heat islands (Morabito et al., 2021; Yao et al., 2021), urban dry islands (Meili et al., 2022; Li et al., 2021) and inundation problems (Huang et al., 2022b; Mu et al., 2020). Moreover, cities encompass unique land surface processes, which differ from those of natural land surfaces. The difference results from the diverse urban configurations, varied building materials, and human interventions (Oh and Sushama, 2021). Therefore, it is necessary to accurately quantify the impacts of urbanization and develop proper mitigation strategies (Yao et al., 2021).

As efficient tools, various land surface models (LSMs) have been rapidly developed in recent decades, providing unprecedented opportunities to obtain detailed information on the storage and movement of surface energy and water cycles (Bierkens et al., 2015). LSMs have been used for various applications, such as land-climate interactions (Zhong et al., 2020; Wang et al., 2020), hydrothermal environment quantifications (Zhao et al., 2019; Huang et al., 2022a), and dataset productions (Hersbach et al., 2020; Rodell et al., 2004). However, LSMs are generally formulated for natural land surfaces (Best and Grimmond, 2015), and often overlook the unique characteristics (e.g., urban configurations and buildings) of urban systems. Specific models should be developed or improved by considering the complexity and uniqueness within cities.

The existing urban parameterization schemes in LSMs mainly involve the bulk approach and coupling with urban canopy models (UCMs) (Ji et al., 2021; Meng, 2015). The bulk approach treats

62   urban surfaces as a regular land cover category with modified thermal and hydrological parameters (e.g.,

63   albedo and infiltration) (Wang et al., 2020; Yang et al., 2010), but still lacks consideration of urban-

64   specific characteristics, such as building blocking, radiative interactions (Salvadore et al., 2015),

65   artificial heating and irrigation (Chen et al., 2022). Coupling LSMs with UCMs (hereafter referred to as

66   LSM-UCMs) is also a popular strategy for capturing land surface processes in urban systems. Various

67   LSM-UCMs have been favorably applied in studies (Meng, 2015; Mcnorton et al., 2021; Yang et al.,

68   2010), including the Met Office–Reading Urban Surface Exchange Scheme (MORUSES) (Simón-

69   Moral et al., 2019), Community Land Model-Urban (CLMU) (Oleson and Feddema, 2020), and

70   Geophysical Fluid Dynamics Laboratory land model LM3 (LM3-UCM) (Li et al., 2016b). However,

71   there remains a shortage of LSM-UCM models, typically oversimplifying the dynamics of land cover

72   and climate change by using constant parameters in simulations (Kusaka et al., 2001).

73   To better represent urban environments, more suitable methodologies are needed (Yao et al., 2021).

74   Among the various LSM models, the Variable Infiltration Capacity (VIC) model is widely used for

75   identifying thermal and hydrological processes on land surfaces (Meng et al., 2019; Meng et al., 2020;

76   Zhu et al., 2020). VIC is characterized by grid-independent calculation and favorable consideration of

77   multiple layers along both horizontal (i.e., land cover types) and vertical (i.e., soil layers) directions

78   (Liang and Xie, 2001; Liang et al., 1996). The model can be coupled with multiple remote sensing data

79   (e.g., shortwave/longwave radiation, albedo, and leaf area index [LAI]) (Jiang et al., 2022; Meng et al.,

80   2020; Wang et al., 2022), to consider the realistic dynamics in land surface properties and atmospheric

81   conditions. The VIC model has been implemented in several urban-related studies based on the bulk

82   approach, and has provided an acceptable performance in simulating energy and hydrological fluxes

83   (Yang et al., 2010; Mishra et al., 2010; Wang et al., 2020). Yet a systematic urban calculation method

84   that considers the unique urban characteristics within VIC is still lacking.

85   In this study, we developed an urban module within the VIC model based on the Urban Tethys-

86   Chloris model (UT&C) (Meili et al., 2020), namely, the VIC-urban model. The coupled model can

87   efficiently identify urban hydrothermal processes when solving the water and energy balance and

88   consider unique urban characteristics, including urban geometry, radiative interactions among urban

89   surfaces (i.e., roof, canyon, walls, and ground), and human interference (e.g., irrigation and inner

90   building temperature). VIC-urban can facilitate multiple urban-related researches, such as identifying

91   long-term hydrothermal processes in urban systems, quantifying environmental changes resulting from

92   urban expansion, and comparing environmental variations among different urban configurations. In this

93   article, we first provide a technical description of the model coupling, process and evaluate the model

94   in Beijing regarding the land surface temperature (LST), turbulent heat fluxes, and runoff. Further, we

95   examine the sensitivity of the urban model input parameters to the urban environment (i.e., roof

96   evaporation and temperature, canyon evaporation and temperature).

2. Methodology

2.1 Urban module coupled with VIC

99   The VIC model divides a study area into Latitude-Longitude grids, with each grid representing

100   multiple land cover types and soil layers. It estimates hydrological and thermal processes for each

101   subgrid land cover type in the solution of water and energy balance (Liang et al., 1994; Liang et al.,

102   1996). However, the existing parameterization scheme ignores the unique characteristics of urban areas, such

103   as building blockage and human influence (e.g., indoor temperature, anthropogenic heat and water inputs).

104   Fortunately, VIC assigns a unique ID number to each grid, and labels each vegetation type within the target

105   grid. This enables VIC to identify and compute the subgrid land cover with individual parameters, offering

106   advantages for establishing the urban module channel.

107   We integrate an urban module into the VIC model (VIC-urban). It executes the urban module for

108   urban tiles, and follows the same calculation routine as the original VIC model for the other land cover

109   tiles. Specifically, the model uses two parameters (i.e., Gridcell and Urban_index) to identify urban tiles,

110   as shown in Figure 1. Gridcell is the ID number of the target grid. Urban_index serves as an index to

111   ascertain the presence of an urban tile, and to identify the urban tile label in the target grid. Urban_index

112   is equal to n-1 if the urban tile is the n_{th} land cover type of the target grid, and equal to -1 if there is no

113   urban tile in the grid. The VIC-urban model can thus identify the target grid and urban tile, and obtain

114   the parameters of the urban tile (i.e., the parameters of the [Urban_index+1]$_{th}$ land cover type in the

115   target grid).

116
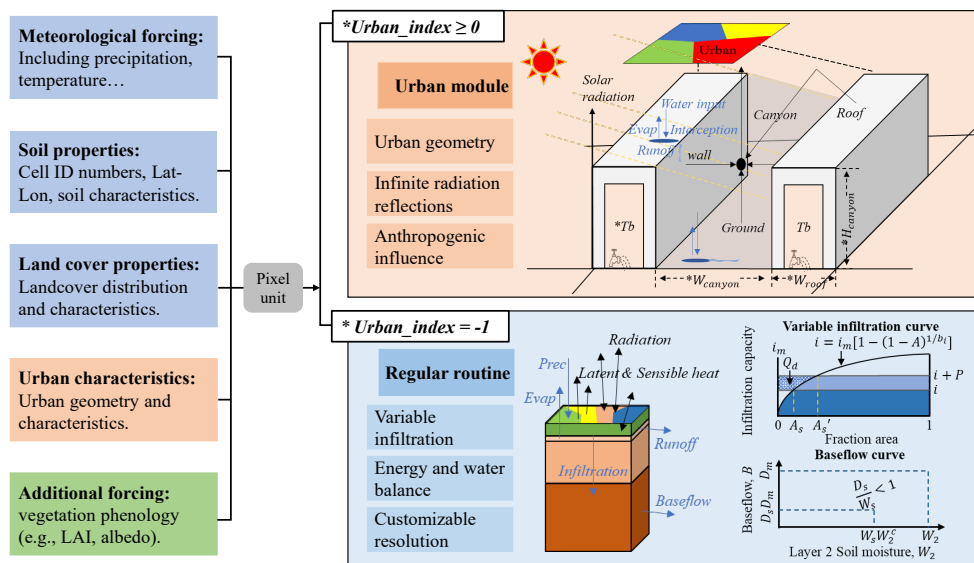
117   **Figure 1.** Diagram of the urban module coupled with the VIC model. *Wcanyon, *Wroof, *Hcanyon are
118   parameters that describe the urban geometry (canyon width, roof width, and canyon height). *Tb is the inner
119   building temperature. The parameters including As and Ds are defined by the original VIC model, and
120   detailed information can be found on the VIC website.

121   The urban module implemented in our study is based on the methods described in Meili et al.

122   (2020). The urban tile is parameterized by three urban geometry parameters (canyon height, canyon

123   width, and roof width) and four urban surfaces (roof, impervious ground, sunlit and shaded walls). The

124   hydrothermal fluxes and states (e.g., turbulent heat fluxes and land surface temperature) are individually

125   calculated for each urban surface, considering the urban geometry, radiative interaction, and water and

126   energy budgets. In addition, the urban module accounts for human impacts, including inner building

127   temperature, and artificial heating and irrigation. We present core formulations of the urban processes

128   and related parameters in Subsections 2.2-2.5. A more detailed explanation is included in the

129   Supplementary Document and Meili et al. (2020).

130   **2.2 Energy balance in the urban module**

131   The newly developed urban module in VIC-urban treats the energy balance differently between

132   the upper (i.e., roof) and lower canyon surfaces (i.e., ground and walls). For the roof surface, both short-

133   and longwave radiation values are calculated similar to those on bare soil, as the model assumes no

134   obstruction or radiative interaction on roofs (Supplementary Section 1.1). For the ground and walls, the

135   model first computes the incoming direct shortwave radiation as a function of the urban geometry, solar

136   position, and grid location (Supplementary Section 1.2). Then, it estimates the temperature, net absorbed

137   radiation, and turbulent fluxes of each surface according to the sky-view factor (Supplementary Section

138   1.5) and infinite radiation reflections among the various surfaces (i.e., ground, sunlit and shaded walls,

139   and sky) based on energy and water budgets. The detailed calculation method for the radiation can be

140   found in Supplementary Section 1, and that for the turbulent fluxes can be found in Supplementary

141   Section 2.

142   The energy balance of the roof, ground and wall can be calculated as:

143    $$EB_i = S_{abs,i} + L_{abs,i} - G_i - H_i - LE_i, \qquad\qquad (1)$$

144   where EB_i is the energy balance of surface i, and $S_{abs,i}$ and $L_{abs,i}$ [W m^{-2}] are the net absorbed short-

145   and longwave radiation values, respectively, of surface *i* (roof, ground, and wall). G_i, H_i, and LE_i are

146   the conductive heat, sensible heat and latent heat fluxes, respectively, of surface *i*, and they can be

147   calculated as:

148    $$H_i = \rho_a C_p \frac{T_i - T_a}{r},$$ (2)

149    $$LE_i = \lambda \rho_a \frac{q_{sat,T_i} - q_a}{r},$$ (3)

150    $$G = -\lambda g \frac{(T_{int} - T_i)}{z},$$ (4)

151   where ρ_a [kg m⁻³] is the air density, C_p [J kg⁻¹ K⁻¹] is the specific heat capacity of air at a constant pressure,

152   T_i [K] is the temperature of surface *i*, [s m⁻¹] is the sum of the resistance values, λ [J kg⁻¹] is the latent heat

153   of vaporization, and q_{sat,T_i} [-] is the saturation specific humidity at temperature T_i. Notably, for the surface

154   above the canyon (i.e., canyon roof), T_a [K] and q_a [-] are the air temperature and specific humidity,

155   respectively, and for the ground and walls, T_a [K] and q_a [-] are the canyon temperature and specific

156   humidity at the canyon reference height, respectively (Supplementary Section 2.5). Moreover, λg [J K⁻

157   ¹ m⁻¹ s⁻¹] is the heat conductivity, and z is the thickness of the layer. T_{int} is the interior building temperature,

158   which can be calculated from the outdoor and indoor temperatures based on the thermal conductivity

159   parameters (Supplementary Section 2.2).

160   The energy balance of an urban canyon can be expressed as:

161    $$EB_{can} = Q_{can} + H_g + h_{can}(H_{wsun} + H_{wshd}) + LE_g - H_{can} - LE_{can},$$ (5)

162   where EB_{can} is the energy balance of the canyon, Q_{can} is anthropogenic heat, H and LE are the sensible

163   heat and latent heat fluxes, respectively, and the subscripts *g, can, wsun*, and *wshd* denote the ground,

164   canyon, sunlit wall, and shaded wall, respectively. h_{can} [-] is the canyon height normalized by the canyon

165   width (H_{can} / W_{can}).

166   The turbulent heat fluxes of canyon can be calculated as the area-weighted average of the walls and

167   ground and directly include the anthropogenic heat input (Equation 6), and the total turbulent fluxes of

168   an urban tile can be calculated as the area-weighted average of the roof and urban canyon (Equation 7):

169    $$X_{can} = w_{can}X_g + h_{can}(X_{wsun} + X_{wshd}) + Q_{can},$$ (6)

170    $$X_{urban} = f_{roof}X_{roof} + f_{can}X_{can},$$ (7)

171   where X [W m^{-2}] denotes the turbulent heat fluxes (i.e., latent or sensible heat fluxes), f_{roof} and f_{can}

172   [-] are the roof and canyon fractions, respectively, and Q_{can} [W m^{-2}] is the anthropogenic heat input.

173   The subscripts *g, can, wsun*, and *wshd* denote the ground, canyon, sunlit wall, and shaded wall,

174   respectively.

2.3 Water balance in the urban module

176   The urban module computes the water mass balance for the roof and ground individually. For the

177   roof, the incoming water is initially consumed by evaporation. Subsequently, runoff occurs when the

178   remaining water exceeds the maximum water interception capacity. Runoff can be further divided into

179   outflow runoff and runon according to a certain ratio defined by experience. Outflow runoff flows off

180   the roof and turns into incoming water for the ground, while runon remains on the roof as the incoming

181   water for the roof at the next time step. Therefore, the incoming water is equal to the precipitation and

182   runon of the previous time step.

183    $$Int_t - Int_{t-1} = P_t + Runon_{t-1} - E_t - Runoff_t - Runon_t,$$ (8)

184   where *Int* [mm h^{-1}] is the interception water, P [mm h^{-1}] is the precipitation, and E [mm h^{-1}] is the

185   evaporation.

186   For the ground, the incoming water flux includes precipitation, roof runoff, anthropogenic water

187   input, and runoff of the previous time step. The incoming water is first consumed by evaporation and

188   leakage and then by runoff and runon. Outflow runoff leaves the current cell, while runon remains in

189   the cell as incoming water of the next time step. Notably, the model does not consider subsurface

190 hydrological fluxes within urban tiles, such as soil moisture and baseflow, since impermeable surfaces

191 impede vertical hydrological interactions. Therefore, the grid-scale subsurface water fluxes are assumed

192 to be equal to the areal-weighted mean value of the fluxes of the other land cover types in the grid.

193 $Int_t - Int_{t-1} = P_t + Runon_{t-1} + Runoff_{t,roof} + Q - E_t - Leak_t - Runoff_t - Runon_t,$ (9)

194 where Q [mm h^{-1}] is the anthropogenic water input.

195 **2.4 Parameters for the urban module**

196 **Table 1.**
197 Overview of datasets for urban module in VIC model

Parameter	Unit	Description
Gridcell	N/A	**Grid cell number**
Urban_index	N/A	**Index of the veg tile containing the urban**, with respect to the list of veg tiles given in the veg param file for the current grid cell. Ranges 0~(Nveg-1) for a grid cell that contain urban, and set to -1 to denote the gird cell exclude urban.
Theta_canyon	°	**Canyon orientation**
Zatm	m	**Atmospheric forcing/reference height**
Qf_canyon	W/m²	**Human interference:** Anthropogenic heat input
Waterf_canyon	mm/h	**Human interference:** Anthropogenic water input
Height_canyon	m	**Urban geometry:** Height of urban canyon
Width_canyon	m	**Urban geometry:** Ground width of urban canyon
Width_roof	m	**Urban geometry:** Roof width of urban canyon
Perrunoff_R/G	N/A	**Water budget:** Percentage of excess water that leaves the roof/ground as runoff
In_max_R/G	mm	**Water budget:** Maximum interception capacity of roof/ground
Kimp_R/G	mm/h	**Water budget:** Hydraulic conductivity of roof/ground
Albedo_R/G/W	N/A	**Energy budget:** Albedo roof/ground/walls
Emissivity_R/G/W	N/A	**Energy budget:** Emissivity roof/ground/walls
Lan_dry_R/G/W	W/(m*K)	**Energy budget:** Thermal conductivity of roof/ground/walls
Cv_s_R/G/W	J/(m³*K)	**Energy budget:** Volumetric heat capacity of roof/ground/walls
Dz1_R/W	m	**Energy budget:** Thickness of first roof/wall layer
Dz2_R/W	m	**Energy budget:** Thickness of second roof/wall layer

198   For the urban module, the input data include land cover maps and urban-related parameters. The

199 land cover maps represent the locations of urban areas. The urban-related parameters are summarized

200 in Table 1. Specifically, the Gridcell and Urban_index parameters are used to identify urban tiles,

201 Qf_canyon and Waterf_canyon denote anthropogenic forcings, and the Theta_canyon, Zatm,

202 Height_canyon, Width_canyon, and Width_roof parameters define the urban geometry. Parameters such

203 as the hydraulic conductivity and maximum interception capacity albedo (i.e., Perrunoff, In_max, and

204   Kimp) are used for water budget calculation, while the other parameters (e.g., albedo, emissivity,

205   Lan_dry, Cv_s, and Dz) are used for energy budget calculation.

206   **2.5 Input data for VIC-urban**

207   In addition to the urban-related parameters listed in Table 1, the other needed input data of the VIC-

208   urban model are similar to those of the original VIC model, referring to Liang et al. (1994), Liang et al.

209   (1996), and Liang and Xie (2001). In general, the input data include topographical, meteorological

210   forcing, soil and land cover (i.e., vegetation) properties. The topographical dataset is used to delineate

211   river networks and interpolate meteorological data. Meteorological forcings provide information on

212   precipitation, maximum and minimum air temperatures, wind speed, and humidity. Soil data define the

213   initial soil moisture conditions, including variable infiltration curve and saturated hydrologic

214   conductivity, and land cover data provide vegetation conditions such as the root zone thickness and the

215   root fraction of each vegetation type.

216   In addition to the needed forcing files, the VIC model can incorporate vegetation and radiation time

217   series data (e.g., LAI, albedo, and shortwave/longwave radiation), which are particularly useful because

218   they provide dynamic information on vegetation and radiation variables. By incorporating these data,

219   the VIC model can better capture realistic land surface dynamics and energy budgets.

220   **3. Case description**

221   **3.1. Study area and data input**

222   The VIC-urban model was evaluated in reproducing observation-based sensible and latent heat,

223   runoff and LST measurements in Beijing. Beijing is the capital of China, located between 39.43-41.05°N

224   and 115.42-117.50°E. The city has experienced rapid urbanization since 1980, with extensive urban

225   coverage since 2000 (Wang et al., 2020). Beijing can be divided into four functional zones with varying

226   degrees of urbanization: the Core Functional Zone (Core-Zone, with an urban fraction of ~90%), the

227   Urban Functional Extended Zone (Extended-Zone, ~70%), the New Urban Development Zone

228   (NewDev-Zone, ~30%), and the Ecological Conservation Zone (Eco-Zone, ~5%) (Figure 2). This

229   evaluation primarily focused on the three highly urbanized zones (Core-Zone, Extended-Zone, and

230   NewDev-Zone) to demonstrate the performance of VIC-urban.

231   The parameters used in the urban module were based on those reported by Jackson et al. (2010),

232   with manual calibration of the height-to-width ratio and the wall layer thickness based on MODIS LST

233   and runoff observation data. The height-to-width ratio is a highly sensitive parameter in LST modelling

234   and ranges from 0.5 to 1.1 according to the MODIS LST product. The prescribed wall layer thickness

235   ranged from 0.2 to 0.6. The values of these parameters are generally consistent with previous research

236   (Mcnorton et al., 2021; Li et al., 2016a), where the height-to-width ratio ranges from 0.75 to 1.5 and the

237   wall layer thickness ranges from 0.3 to 0.5.

238   Regarding the model input data of Beijing, topographical data (i.e., the digital elevation model)

239   were obtained from the USGS with a 90-m resolution. Meteorological forcing data were produced by

240   interpolating the data obtained from observation stations of the China Meteorological Administration

241   (CMA) (Xie et al., 2015; Zhu et al., 2021). A soil map was obtained based on a 30 arc-second-resolution

242   soil characteristics dataset. The soil parameters were derived based on a Chinese soil dataset (Shangguan

243   et al., 2013; Zhu et al., 2020) and Food and Agriculture Organization (FAO) (Nijssen et al., 2001). The

244   land cover maps included base maps and urban maps. The base maps were obtained from Liu et al.

245   (2010), which were created by merging Landsat TM digital images with a spatial resolution of 1 km and

246   12 land cover types. The urban maps were obtained from Wang et al. (2020), which were created by the

247   Classification Regression Tree (CART) method using Landsat images with a spatial resolution of 30 m.

248   The land cover parameters were obtained from Zhu et al. (2020). Moreover, four satellite datasets,

249   namely, Downward Shortwave Radiation (DSR), albedo, LAI, and Fraction of Vegetation Cover (FVC),

250   were incorporated in the modelling process (Zhang et al., 2019; Liang et al., 2021) to better identify land

251   conditions and calculate turbulent heat fluxes. The four datasets used in this study are at 0.05° spatial

252   resolution. The DSR dataset is at daily temporal resolution, while the other three datasets are at 8-day

253   temporal resolution. The four datasets were obtained from Global Land Surface Satellite (GLASS)

254   products (http://www.geodata.cn/thematicView/GLASS.html) (Liang et al., 2021).

255   **3.2 Evaluation data and method**

256   The VIC-urban model underwent calibration using streamflow data from two watersheds and

257   MODIS-based LST data. Then, it was validated against observations retrieved from gauge stations and

258   MODIS data regarding sensible and latent heat, runoff, and LST. The locations of the gauge stations are

259   shown in Figure 2, and detailed information is listed in Table 2. Four measures, namely, the Nash–

260   Sutcliffe efficiency (*NSE*), Root Mean Squared Error (*RMSE*), relative bias (*Er*), and correlation

261   coefficient (*R*) were used to evaluate the performance of VIC-urban.

262   In regard to sensible and latent heat evaluation, three flux towers were used, namely, the Beijing,

263   Daxing, and Miyun stations. In particular, the Beijing station is located in the central part of Beijing and

264   is widely used to investigate urban turbulence characteristics (Liu et al., 2020b; Ji et al., 2021). To

265   calibrate and validate the simulated runoff, streamflow data from three stations were used, namely,

266   Boyachang (BYCH), Qianxinzhuang (QXZH), and Wenyu (WY). Their corresponding watersheds are

267   located in the northern part of Beijing and contain various land cover types, including urban, forest, crop,

268   and grass (Figure 2). The observed discharge data of the QXZH and BYCH stations were separated into

269   two periods for model calibration and validation, whereas the observed discharge of the WY station was

270   compared to the simulated runoff for the entire period due to the availability of only yearly data.

271   **Table 2.**

272   Validation data used in this work

Name	Source	Detailed information
Sensible heat	NCDDC, IAP	Beijing, 2011-2013, daily
Latent heat	NCDDC, IAP	Beijing, 2011-2013, monthly Miyun, 2018-2010, daily
Runoff	AHRPR	Daxing, 2018-2010, daily QXZH, 2006-2009, monthly BYCH, 2006-2014, monthly
LST	CMA, MODIS	WY, 2005-2017, yearly 14 ground stations, daily MOD11A2, eight-days

NCDDC, National Cryosphere Desert Data Center; IAP, Institute of Atmospheric Physics; AHRPRC, Annual Hydrological Report for the P.R. China, CMA, China Meteorological Administration; MODIS, MODerate-resolution Imaging Spectroradiometer; QXZH, Qianxinxhuang; BYCH, Boyachang; WY, Wenyu.
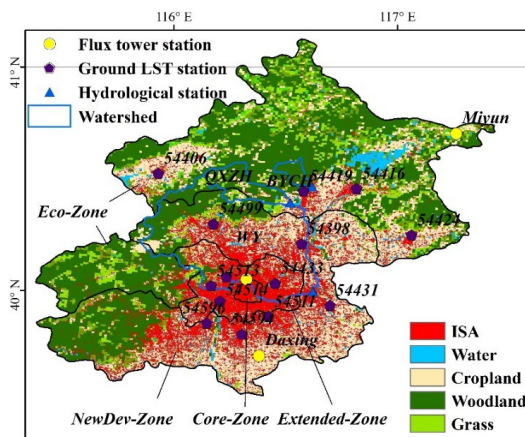
273

274   **Figure 2.** Location of Beijing and the flux tower stations, hydrological stations and watersheds, and ground
275   LST stations, with the 2015 land cover map as the background.

276   Regarding LST evaluation, we obtained data from fourteen ground-based stations and one satellite-

277   based product. At the ground-based stations of the CMA, platinum resistance sensors are used that are

278   semi-buried in soil to measure the daily temperature at the skin surface. Among the stations, three

279   stations provide long-term coverage data for the 2005 to 2020 period, while the remaining stations

280   provide data covering the 2016 and 2020 period. The satellite-based LST product of the Terra Moderate

281   Resolution   Imaging   Spectroradiometer   (MODIS)   was   adopted,   i.e.,   MOD11A2   v006

282   (https://modis.gsfc.nasa.gov/). MODIS LST data constitute one of the most widely used data for LST

283   studies (Bounoua et al., 2015; Zhou et al., 2010; Liu et al., 2020a; Morabito et al., 2021; Zhou et al.,

284   2018). The MODIS has provided two instantaneous LST estimates (10:30 and 22:30 local solar time)

285   every eight days since 2000, with a spatial resolution of 1 km. In our work, the simulated LST was

286   averaged every eight days for comparison with the MODIS data. The simulated LSTs from 9:00-12:00

287   and 21:00-24:00 were compared with the MODIS data for 10:30 and 22:30, assumed to represent the

288   morning and evening times, respectively. Notably, the gauge-based measurements were obtained at the

289   point scale, which is smaller than the model output resolution. To resolve the mismatch in the spatial

290   scale, the evaluation was conducted at the subgrid scale with the same land cover type in the

291   corresponding grid.

292   **3.3 Sensitivity analysis**

293   To examine the sensitivity of the model parameters to changes in the urban environment. Four

294   fluxes, namely, roof temperature, roof evaporation, canyon temperature, and canyon evaporation, were

295   used as indicators of the urban environment. A single grid cell with high urban coverage was selected,

296   and its input values were used as default values. The urban input parameters range from 70% to 130%

297   of the default values in 6% change steps. The specific parameters and their values are listed in

298   Supplementary Table 1.

299   The sensitivity analysis covered 6 years (2015-2020) and was conducted at the annual scale, as

300   well as for the winter (December to February of the next year) and summer (June to August) seasons.

301   The sensitivity coefficient Sc can be calculated as (Beven, 1979):

302    $$Sc = \lim_{X \to 0} \frac{\Delta Y / Y}{\Delta X / X} \times 100\%, \tag{10}$$

303   where X is the input parameter that affects the urban environment (Y). A positive (or negative) Sc value

304   suggest that Y is enhanced (or reduced) with increasing X.

4. Results

4.1 Land surface temperature

The simulated LST was calibrated against the MODIS LST and evaluated using two ground observations and the MODIS LST dataset. As shown in Figure 3, the simulated LST exhibited similar spatial patterns to those of the MODIS estimates for both the morning and evening times at the city center. At the morning time, both the VIC-urban model and MODIS data exhibited high LST values in Core-Zone and the southern part of Extended-Zone. At the evening time, the VIC-urban model simulations failed to capture the scattered LST patterns in Eco-Zone and the southwestern part of NewDev-Zone. This disagreement may be attributed to the relatively low urban fraction in these areas, given that our work mainly focused on the calculation of urban-related processes. Other than in these areas, the model could accurately produce a similar LST distribution relative to the MODIS LST data in Core-Zone and Extended-Zone.

In terms of temporal comparison, the simulated LST exhibited a high performance in all of Beijing and the three subzones (Core-Zone, Extended-Zone, and NewDev-Zone). As shown in Figures 4 and 5, the simulated LST indicated similar yearly dynamics and mean monthly cycles relative to the MODIS LST data. The R values were over 0.8, and the $RMSE$ and Er values were lower than 0.5℃ and 2.3% for the morning and evening times, respectively. These results indicated that the simulated LST values closely captured the temporal variations and spatial patterns of the MODIS LST data for Beijing and the three subzones.

324
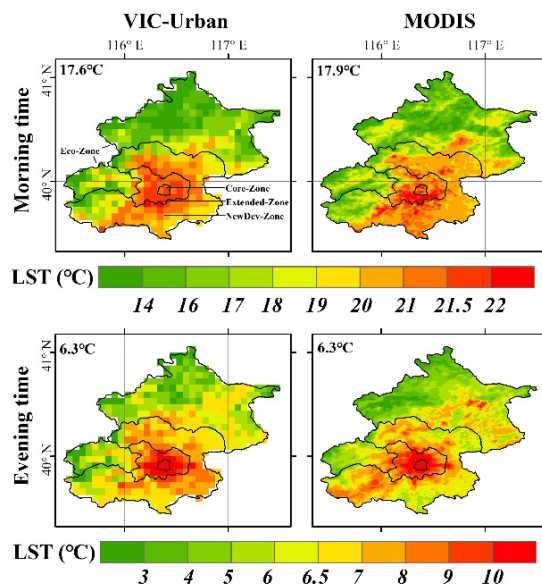
Figure 3. Spatial distribution of the simulated LST compared to the MOD11A2 product, with the average

LST shown in the upper left of the figure.

327
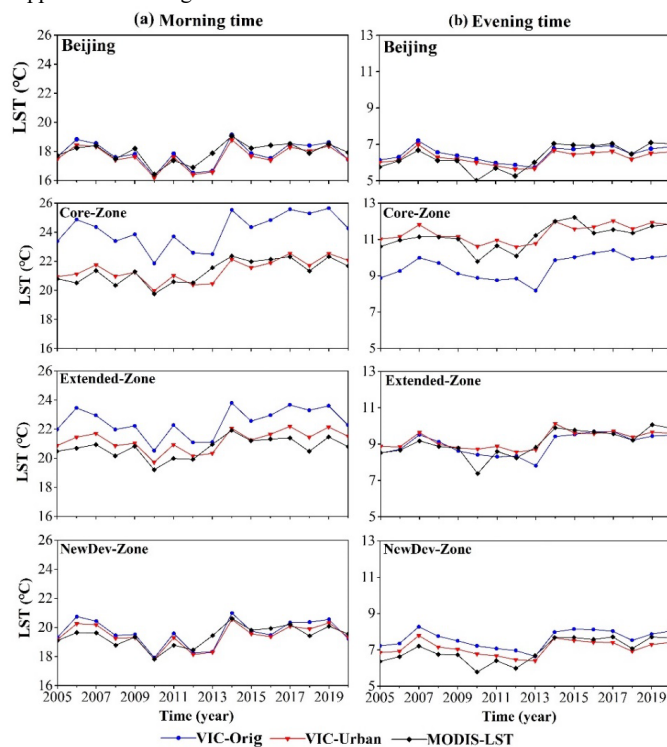
Figure 4. Yearly dynamics of the simulated LST compared to the MOD11A2 product for Beijing and the

three functional zones (i.e., Core-Zone, Extended-Zone, and NewDev-Zone).
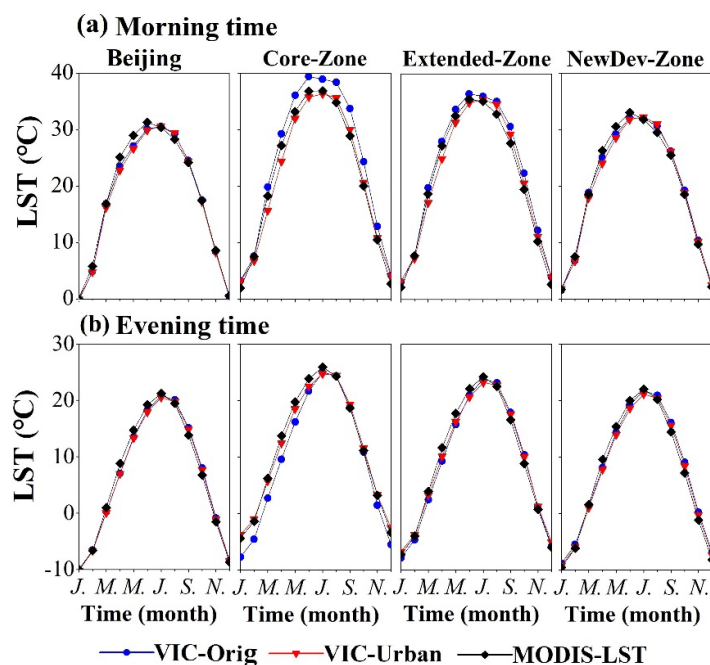
Figure 5. Mean monthly cycle of the simulated LST compared to the MOD11A2 product for Beijing and the three functional zones (Core-Zone, Extended-Zone, and NewDev-Zone).

In regard to station-scale comparison, the model produced satisfactory LST estimates for the annual dynamics and during the winter and summer seasons (Figure 6). Specifically, the overall *RMSE* was lower than 1.9 °C, *R* was higher than 0.9, and *Er* was lower than 7% at the annual scale. During the winter and summer seasons, the *RMSE* values were lower than 1.7 °C, the *R* values were higher than 0.7, and *Er* was approximately 24.9% in winter and −0.2% in summer. The high *Er* value during the winter season could be attributed to the low average winter LST. The comparison at each site also indicated promising results (Table 3), with all *Er*s values lower than 12% and all *RMSE* values below 1.8 °C. It is important to note that the stations generally provided only five available values, i.e., annual data for the 2016 to 2020 period. Nevertheless, the *R* values for all the stations consistently exceeded 0.4, indicating the satisfactory performance of the VIC-urban model.
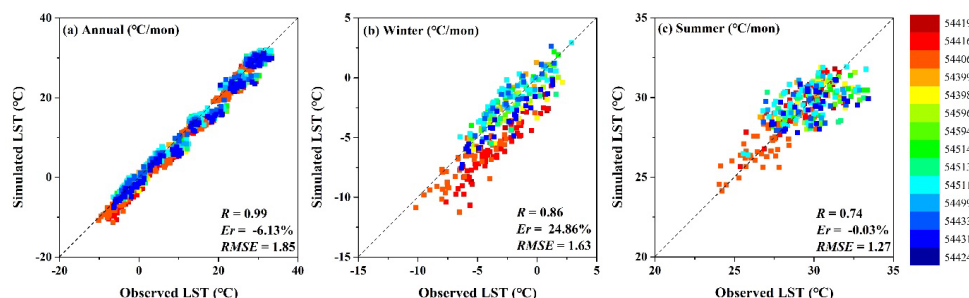
Figure 6. Monthly simulated LST validated against 14 ground-based observation stations, which are marked in different colours.

Table 3.
The simulated LSTs from VIC-urban and VIC-orig models are validated by 14 ground-based observations at an annual scale. The results of three indexes (*Er*, *R* and *RMSE*) are shown in the table, with the better results underlined.

Station	*Er (%)*		*R*		*RMSE*	
	VIC-urban	VIC-orig	VIC-urban	VIC-orig	VIC-urban	VIC-orig
54419	−7.78	-9.56	0.64	0.15	1.19	1.47
54416	−11.28	-10.58	0.79	0.89	1.63	1.52
54406	−8.37	-12.75	0.87	0.65	1.06	1.64
54399	0.29	8.61	0.92	0.69	0.12	1.28
54398	−8.24	-13.54	0.61	0.56	1.34	2.17
54596	-6.54	-5.29	0.63	0.68	1.07	0.88
54594	-7.10	-3.77	0.48	0.92	1.13	0.60
54514	-5.21	1.18	0.92	0.73	0.84	0.28
54513	-5.46	-3.54	0.80	0.51	0.85	0.67
54511	−1.38	-3.97	0.73	0.34	0.61	2.00
54499	−1.88	-1.71	0.88	0.72	0.37	0.40
54433	−0.87	3.09	0.40	0.38	0.35	0.58
54431	−5.24	-7.59	0.85	0.01	0.85	1.24
54424	−11.74	-12.44	0.77	0.46	1.76	1.88

4.2 Runoff

The model was further calibrated using the streamflow data for the QXZH and BYCH watersheds and validated against the streamflow data for the WY, QXZH, and BYCH watersheds (Figure 7). During the calibration period, the *NSE* and *R* values for the QXZH and BYCH watersheds were approximately 0.5 and 0.8, respectively, and the *Er* and *RMSE* values were below 10% and 4 mm/month, respectively, for both watersheds. During the validation period, the simulated runoff showed a high correlation with the observed data of the three watersheds, with *R* ranging from 0.8 to 0.9 and *NSE* ranging from 0.6 to 0.8. The *RMSE* reached approximately 4 mm/month at QXZH, 5 mm/month at BYCH, and 42 mm/yr

358   at WY. The *Er* values were approximately 12% (QXZH), 29% (BYCH), and −9.5% (WY), respectively.

359   The overestimations at QXZH and BYCH and the underestimation at WY could likely be attributed

360   to the limitations of the VIC-urban model in considering human activities. Specifically, the model did

361   not consider water allocation for industrial use in the upstream region of the city (QXZH and BYCH)

362   or the impact of industrial and domestic wastewater at the city centre (WY). *Er* of the WY watershed

363   showed an increasing trend, particularly after 2013, which could be attributed to the increasing

364   wastewater discharge. Despite these limitations, the VIC-urban model demonstrated an acceptable

365   performance in simulating runoff.
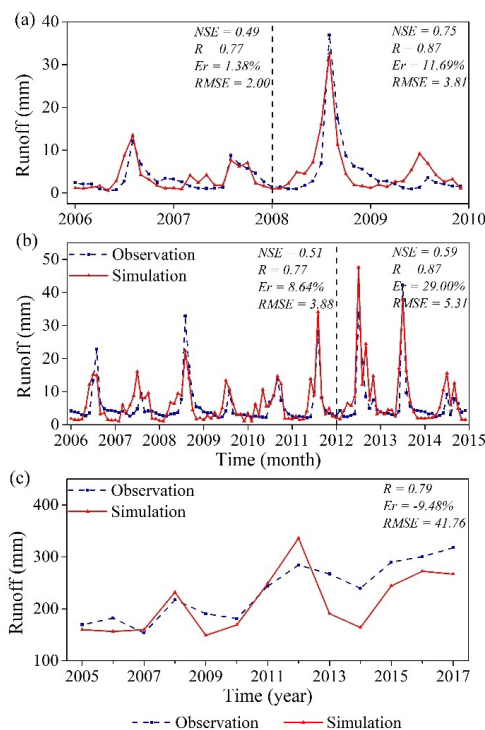
366
367   **Figure 7.** Evaluation of the simulated runoff. (a) QXZH; (b) BYCH; and (c) WY. The dark dotted line
368   divides the data into the calibration period (before) and validation period (after).

369   **4.3 Turbulent heat fluxes**

370   The VIC-urban model was evaluated regarding the sensible and latent heat using the observed

371   data of three stations: Beijing, Miyun, and Daxing. As shown in Figure 8a, the simulated sensible heat

372   flux agrees well with the observed value at the Beijing station. R is approximately 0.65, and the $RMSE$

373   and Er are below 22 W/m^2 and 25%, respectively. Regarding the latent heat (Figure 8b, c, d), the

374   simulated values exhibit high correlations (Rs) with the observed data at the Beijing and Miyun

375   stations (~ 0.86), and R at the Daxing station is approximately 0.65. Additionally, the $RMSE$ values

376   are below 30 W/m^2 for all stations, and the Er values vary between −21% and −17%.
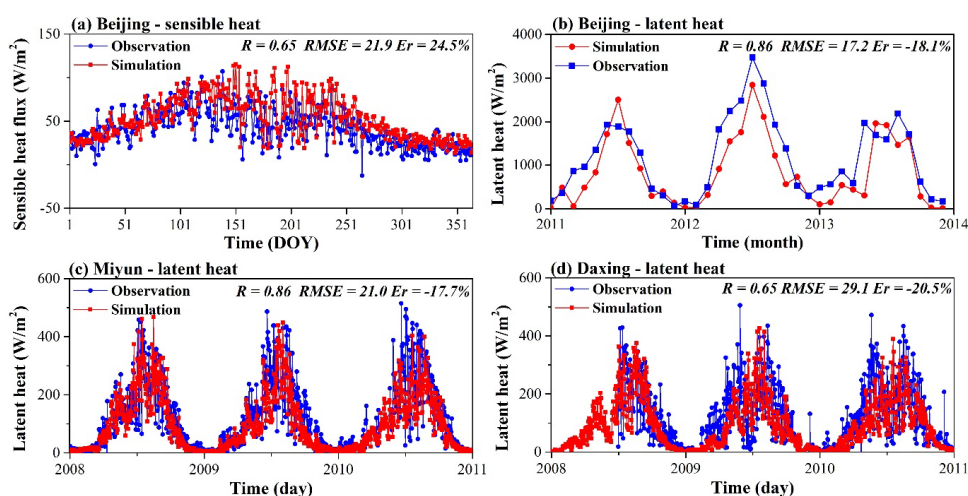
377

378 **Figure 8.** Evaluation of the sensible and latent heat flux simulations. (a) Sensible heat flux at the Beijing
379 flux tower; (b) latent heat flux at the Beijing flux tower; (c) latent heat flux at the Miyun flux tower; (d) latent
380 heat flux at the Daxing flux tower.

381   **4.4 Comparison with the original VIC**

382   The performance of the VIC-urban model and the original VIC model (VIC-orig) were compared

383   in terms of the simulated turbulent heat fluxes, LST, and runoff. As shown in Figure 9, the simulation

384   results of the VIC-urban and VIC-orig models showed similar patterns at the Miyun and Daxing stations.

385   However, at the Beijing station, with a high degree of urbanization, the VIC-urban model provided a

386   better performance for both the latent heat and sensible heat fluxes. Specifically, the VIC-urban model

387   yielded a smaller $RMSE$ (~21.2 W/m^2) for the latent heat flux than that of the VIC-orig model (~35.4

388   W/m^2) and attained a higher correlation with the observed sensible heat flux (*R* of 0.92) than the VIC-

389   orig model (R of 0.81) at the Beijing site.

390   In terms of the LST, the VIC-urban model simulations show a lower discrepancy from the MODIS

391   product, especially at the city centre, and the average LST difference is less than 0.5 °C for both the

392   morning and evening times (Figure 10). However, the average LST difference is larger than 1.8 °C when

393   using the VIC-orig model. Regarding temporal comparison (Figures 3 and 4), the VIC-urban model

394   simulations show similar patterns to those in the MODIS data, while the VIC-orig model simulations

395   tend to overestimate the LST at the morning time and underestimate the LST at the evening time in

396   Extended-Zone. The VIC-urban model also outperforms the VIC-orig model at the station scale, as

397   indicated by the higher *R* and lower *Er* and *RMSE* values (Table 3).
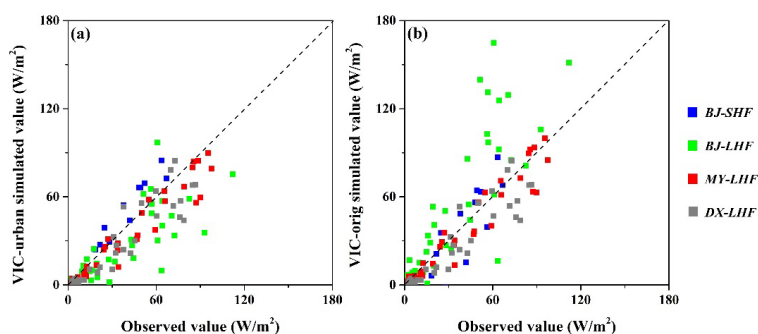
398
399   **Figure 9.** Simulated yearly turbulence heat fluxes of the VIC-urban and VIC-orig models compared to the
400   observed data. The blue points denote the comparison of the sensible heat flux at the Beijing station, and the
401   green, red and grey points denote the comparisons of the latent heat flux at the Beijing, Miyun, and Daxing
402   stations, respectively.

403   Regarding runoff (Figure 11), the VIC-urban and VIC-orig models exhibit similar performance

404   levels for both the BYCH and QXZH watersheds. However, the VIC-orig model obviously

405   underestimates runoff in the WY watershed, which has a high urban coverage. The *RMSE* values of the

406   VIC-orig and VIC-urban model simulations for WY are 98.3 and 41.8 mm/yr, respectively. Based on

407   the comparisons above, it is evident that the VIC-urban model outperforms the original VIC model in

408   analysing urban-related processes and can capture more realistic hydrological and thermal processes in

409   cities.
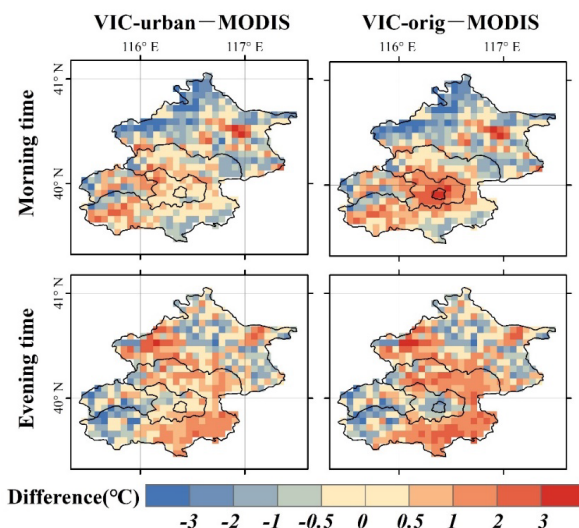
410

411   **Figure 10.** Spatial distribution of the LST differences between the MODIS LST and the simulated LST of
412   the VIC-urban model (left), and between MODIS LST and the simulated LST of the VIC-orig model.
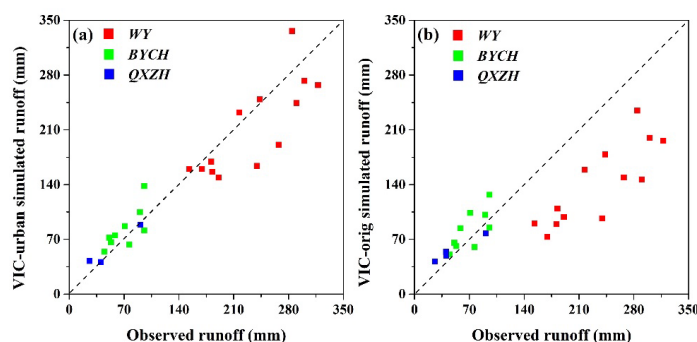
413

414   **Figure 11.** Simulated yearly runoff of the VIC-urban and VIC-orig models compared to the observed data.
415   The red, green, and blue points denote the comparisons in the WY, BYCH, and QXZH watersheds,
416   respectively.

417   **4.5 Sensitivity analysis**

418   We further calculated the sensitivity of the hydrothermal process-related urban input parameters,

419   that is, we calculated the impact on four indicators (i.e., roof temperature and evaporation and canyon

420   temperature and evaporation). Regarding the roof (Figure 12 a, b), Emissivity_R and Albedo_R

421 generally exhibited high sensitivity to the roof temperature, with sensitivity coefficients of −21% and

422 −11%, respectively. The changes in In_max_R, Perrunoff_R, Emissivity_R and Albedo_R exerted

423 obvious impacts on roof evaporation, with values of 41%, −19%, −10%, and −8%, respectively.

424   Regarding the sensitivity of the canyon environment (Figure 12 c, d), Width_canyon (−5%) and

425 Width_roof (4%) imposed the greatest impact on the canyon temperature, followed by Emissivity_W

426 (−4%), Dz_W (−3%), Lan_dry_W (3%), and Albedo_W (−2%). In terms of canyon evaporation,

427 Width_canyon (44%) and In_max_G (37%) yielded the highest impact, followed by Perrunoff_G

428 (−29%), Kimp_G (−23%), Albedo_G (−20%), Emissivity_W (16%) and Albedo_W (14%). An

429 interesting finding is that the wall parameters (e.g., Emissivity_W, Albedo_W) generally imposed a

430 greater influence on the canyon temperature, while the ground parameters exerted a higher influence on

431 canyon evaporation. The sensitivity coefficients of all parameters are listed in Supplementary Table 2.

432   Supplementary Figures 1 and 2 show the urban environment (roof and canyon temperature and

433 evaporation) changes with increasing parameter value during the summer and winter seasons. The urban

434 environment exhibited diverse patterns under parameter increase, rather than simply following linear

435 trajectories. An interesting discovery is that the Dz_R and Lan_dry_R parameters showed opposite

436 impacts on the roof temperature during the summer and winter seasons. This inconsistency could be

437 attributed to their role in regulating heat transfer between indoor and outdoor environments. Specifically,

438 indoor temperatures are higher than outdoor temperatures in winter and lower in summer. A higher

439 thermal conductivity (i.e., higher Lan_dry_R and lower Dz_R values) will increase the outdoor surface

440 temperature in winter and decrease it in summer. Similarly, the parameters related to heat conduction

441 (e.g., Dz_W and Lan_dry_G) in canyon exerted contrasting impacts on the canyon environment during

442 the summer and winter seasons. Moreover, parameters such as albedo and emissivity directly exerted

443 negative impacts on both the roof and canyon temperatures and evaporation levels. Their effects on roofs

444 are generally similar between winter and summer, and their impact on canyons is more pronounced in

445 summer than in winter.

446
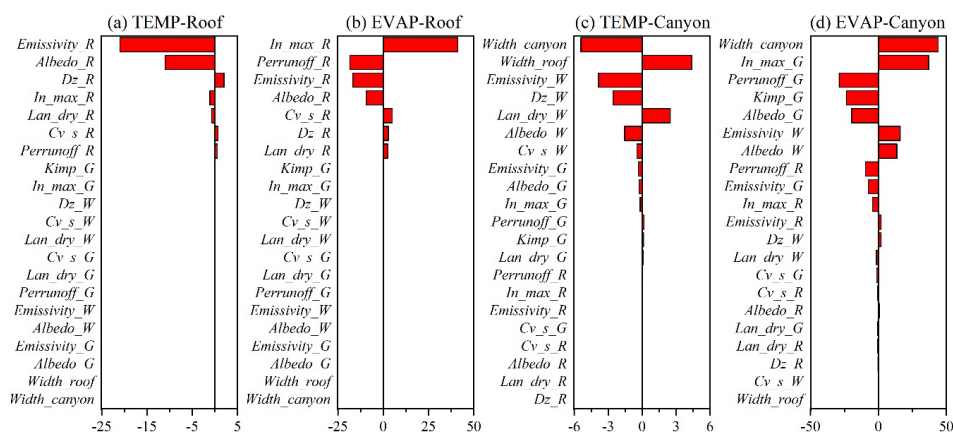
Figure 12. Sensitivity coefficients of the parameters to the urban environment: (a) Roof temperature; (b) roof
evaporation; (c) canyon temperature; and (d) canyon evaporation.

5. Discussion

5.1. Enhanced performance of VIC-urban in urban systems

451   The urban module described above is among the first attempts to establish a systematic urban

452 environment in the solution of the energy and water budget in the VIC model. The VIC-urban model

453 incorporates detailed representations of urban canyons, urban geometry, and human influences. The

454 model therefore provides favourable estimates of various components of the energy and water balance

455 (e.g., surface runoff, evaporation, and LST) of each urban surface (i.e., roof, canyon, ground, and sunlit

456 and shaded walls).

457   In each urban tile, the VIC-urban model calculates the incoming radiation of each surface based on

458 geographic information, solar time, and geometric parameters. It then estimates energy budgets using

459 an iterative approach that considers radiative interactions and energy balance principles(Meili et al.,

460   2020). In water balance calculation, the model simulates the hydrological processes of the ground and

461   roof individually and assumes that roof runoff contributes to the groundwater input. Additionally, given

462   the distinct characteristics of urban areas, where excess water on a given surface tends to remain in place

463   rather than immediately exiting the system (e.g., flat roofs and ground), the model includes a runon

464   component to more comprehensively represent water movement in urban environments.

465   The VIC-urban model was assessed based on the data of multiple gauge stations and MODIS LST

466   data and compared to the original VIC model in Beijing urban areas. The results indicated that the VIC-

467   urban model achieves excellent performance, with *RMSE* values below 0.5 and 1.8 °C relative to the

468   MODIS LST and gauge station data, respectively, and lower than 30 W/m^2 and 6 mm/month in turbulent

469   heat and runoff evaluation, respectively. Importantly, the VIC-urban model outperforms the original VIC

470   model in urban areas. It largely reduces the discrepancy between the simulated and observed values,

471   successfully capturing higher LST and runoff values at the urban center. These findings suggest that the

472   VIC-urban model is a valuable tool for reliable analysis of urban areas.

473   **5.2 Advantages of the VIC-urban model**

474   The development of the VIC-urban model provides a new urban modelling option. It employs the

475   canyon concept, which has been widely used in UCMs and coupled models (Oleson and Feddema, 2020;

476   Li et al., 2016a; Sun and Grimmond, 2019). Compared to UCMs, which often neglect heterogeneity

477   within urban areas (Kusaka et al., 2001; Meili et al., 2020). The VIC-urban model offers high

478   customizability with urban configurations and simulates hydrothermal processes at the grid cell scale.

479   It can merge hydrothermal inputs at the subcity scale to enhance its potential for accurately predicting

480   the water and energy balance in complex urban systems.

481   Large-scale urban models provide advantages in detecting hydrothermal dynamics in urban

482   environments due to their consideration of surface heterogeneity within a city. For instance, the CLMU

483   model incorporates a building energy model that considers convection and longwave radiation exchange

484   with interior building surfaces (Oleson and Feddema, 2020). The LM3-UCM model can simulate carbon

485   exchange and considers dynamic transitions between urban, agricultural, and unmanaged tiles (Li et al.,

486   2016a). However, these models often use constant land cover and radiation parameters over time. The

487   VIC-urban model can continuously capture land cover and radiation dynamics by integrating remote

488   sensing products. Furthermore, it incorporates a comprehensive thermally conductive framework that

489   considers three distinct layers (i.e., outdoor environment, interior building, and indoor environment) and

490   two vertical wall layers. These features are crucial for identifying long-term urban-induced

491   environmental changes and providing a comprehensive understanding of the urban environment.

492   **5.3 Limitations**

493   The current version of the VIC-urban model still has certain limitations. First, the model lacks the

494   water and energy balance related to snow melting, as well as certain anthropogenic disturbances (e.g.,

495   drainage systems, air conditioning, and car exhaust) (Liu et al., 2021). These factors may impose a

496   significant impact on the urban environment and need to be further studied and incorporated into the

497   model. Second, the model does not consider horizontal interactions between land cover types and water

498   and energy transfer in the subsoil beneath impervious surfaces due to impermeable characteristics.

499   Third, the module does not explicitly formulate the type of urban vegetation (i.e., vegetation or

500   trees in cities), which may play an important role in the hydrology and energy cycle of cities (Meili et

501   al., 2020; Wang et al., 2018). Nevertheless, the VIC-urban model divides the study area of interest into

502   grids and categorises urban vegetation as forests and/or grasslands, thus estimating the water and energy

503   balance. Moreover, the VIC-urban model introduces new parameters (Table 1) that should be estimated

504   or calibrated before the simulation, and these parameters may cause substantial uncertainties. Notably,

505   parameters such as In_max_R (maximum infiltration rate) and height-to-width ratio are influential on

506   estimating urban temperature and evaporation patterns, as illustrated in Subsection 4.5. Cities worldwide

507   exhibit diverse configurations and various human influences, leading to differing empirical parameters

508   of influence. The VIC-urban model therefore requires more evaluations in cities with diverse urban

509   environments.

6. Conclusion

511   In this study, we developed a new urban module in the VIC model, demonstrated its reliability and

512   estimated the sensitivity of the model parameters. Adopting Beijing as an evaluation site, the VIC-urban

513   model showed promising performance regarding the simulation of sensible heat, latent heat, runoff, and

514   LST. Moreover, the VIC-urban model could better capture the LST and runoff patterns at the city centre

515   than the original VIC model. The sensitivity analysis revealed that the parameters of emissivity (i.e.,

516   Emissivity_R) and maximum interception capacity of the roof (i.e., In_max_R) generally exert the

517   greatest impacts on the roof temperature and evaporation, respectively, and the height-to-width ratio

518   imposed the highest impact on the canyon temperature and evaporation.

519   The current version of the VIC-urban model still holds substantial uncertainties due to its

520   parameters and related processes and the lack of consideration of human disturbances such as horizontal

521   interactions, air-conditioning systems and snow dynamics. However, our work is among the first

522   attempts to establish a systematic urban estimation within the VIC model, and the model is suitably

523   formulated with detailed subcity configurations, human influences, and radiative balance and

524   interactions. By considering the unique characteristics of urban areas and land cover and radiation

525   dynamics, the VIC-urban model provides a more realistic representation of urban hydrology and thermal

526   dynamics. Therefore, the model can be a valuable tool for detecting and understanding water and energy

527   processes in urban areas, and for improving the prediction of hydrothermal fluxes and states of the urban

528   environment.

529   **Code and data availability**

530   The codes of the VIC-urban, and example file for urban parameters are available at

531   https://doi.org/10.5281/zenodo.10258321.   The   original   VIC   model   is   available   at

532   https://vic.readthedocs.io/en/master/Overview/ModelOverview/,   and   the   urban   module   refers   to

533   https://doi.org/10.5194/gmd-13-335-2020 (Meili et al., 2020). The MODerate-resolution Imaging

534   Spectroradiometer (MODIS) datasets used in this study are available at https://modis.gsfc.nasa.gov/. The

535   Global LAnd Surface Satellite (GLASS) products are available at www.glass.umd.edu.

536   **Author contributions**

537   Yibing Wang designed and implemented the model, performed the analysis, and wrote the manuscript.

538   Xianhong Xie proposed and supervised the study, wrote and revised the manuscript. Bowen Zhu, Arken

539   Tursun, Fuxiao Jiang created the figures and wrote Supplementary Section 1. Yao Liu, Dawei Peng, Buyun

540   Zheng wrote Supplementary Section 2. All authors gave comments and discussions to the study.

541   **Competing interests**

542   The contact author has declared that neither of the authors has any competing interests.

543   **Acknowledgement**

544   This study was supported by grants from the National Natural Science Foundation of China (No.

545   42271021) and Open Fund of State Key Laboratory of Remote Sensing Science and Beijing Engineering

546   Research Center for Global Land Remote Sensing Products (No. OF202204).

547   **Reference**

548   Best, M. J. and Grimmond, C. S. B.: Key conclusions of the first international urban land surface model comparison

549   project, Bulletin of the American Meteorological Society, 96, 805–819, https://doi.org/10.1175/BAMS-D-14-
550   00122.1, 2015.

551   Beven, K.: A sensitivity analysis of the Penman-Monteith actual evapotranspiration estimates, Journal of
552   Hydrology, 44, 169-190, 1979.

553   Bierkens, M. F. P., Bell, V. A., Burek, P., Chaney, N., Condon, L. E., David, C. H., de Roo, A., Döll, P., Drost, N.,
554   Famiglietti, J. S., Flörke, M., Gochis, D. J., Houser, P., Hut, R., Keune, J., Kollet, S., Maxwell, R. M., Reager,
555   J. T., Samaniego, L., Sudicky, E., Sutanudjaja, E. H., van de Giesen, N., Winsemius, H., and Wood, E. F.:
556   Hyper-resolution global hydrological modelling: what is next?, Hydrological Processes, 29, 310-320,
557   10.1002/hyp.10391, 2015.

558   Bounoua, L., Zhang, P., Mostovoy, G., Thome, K., Masek, J., Imhoff, M., Shepherd, M., Quattrochi, D., Santanello,
559   J., Silva, J., Wolfe, R., and Toure, A. M.: Impact of urbanization on US surface climate, Environmental
560   Research Letters, 10, 084010, 10.1088/1748-9326/10/8/084010, 2015.

561   Chen, J., Bu, J., Su, Y., Yuan, M., Cao, K., and Gao, Y.: Urban evapotranspiration estimation based on
562   anthropogenic activities and modified Penman-Monteith model, Journal of Hydrology, 610, 127879,
563   10.1016/j.jhydrol.2022.127879, 2022.

564   Hersbach, H., Bell, B., Berrisford, P., Hirahara, S., Horányi, A., Muñoz‐Sabater, J., Nicolas, J., Peubey, C., Radu,
565   R., Schepers, D., Simmons, A., Soci, C., Abdalla, S., Abellan, X., Balsamo, G., Bechtold, P., Biavati, G.,
566   Bidlot, J., Bonavita, M., Chiara, G., Dahlgren, P., Dee, D., Diamantakis, M., Dragani, R., Flemming, J., Forbes,
567   R., Fuentes, M., Geer, A., Haimberger, L., Healy, S., Hogan, R. J., Hólm, E., Janisková, M., Keeley, S.,
568   Laloyaux, P., Lopez, P., Lupu, C., Radnoti, G., Rosnay, P., Rozum, I., Vamborg, F., Villaume, S., and Thépaut,
569   J. N.: The ERA5 global reanalysis, Quarterly Journal of the Royal Meteorological Society, 146, 1999-2049,
570   10.1002/qj.3803, 2020.

571   Huang, S., Zhang, X., Yang, L., Chen, N., Nam, W.-H., and Niyogi, D.: Urbanization-induced drought modification:
572   Example over the Yangtze River Basin, China, Urban Climate, 44, 101231, 10.1016/j.uclim.2022.101231,
573   2022a.

574   Huang, S., Zhang, X., Yang, L., Chen, N., Nam, W.-H., and Niyogi, D.: Urbanization-induced drought modification:
575   Example over the Yangtze River Basin, China, Urban Climate, 44, 10.1016/j.uclim.2022.101231, 2022b.

576   Jackson, T. L., Feddema, J. J., Oleson, K. W., Bonan, G. B., and Bauer, J. T.: Parameterization of Urban
577   Characteristics for Global Climate Modeling, Annals of the Association of American Geographers, 100, 848-
578   865, 10.1080/00045608.2010.497328, 2010.

579   Ji, P., Yuan, X., Liang, X. Z., Jiao, Y., Zhou, Y., and Liu, Z.: High‐Resolution Land Surface Modeling of the Effect
580   of Long‐Term Urbanization on Hydrothermal Changes Over Beijing Metropolitan Area, Journal of
581   Geophysical Research: Atmospheres, 126, 10.1029/2021jd034787, 2021.

582   Jiang, F., Xie, X., Wang, Y., Liang, S., Zhu, B., Meng, S., Zhang, X., Chen, Y., and Liu, Y.: Vegetation greening
583   intensified transpiration but constrained soil evaporation on the Loess Plateau, Journal of Hydrology, 614,
584   128514, 10.1016/j.jhydrol.2022.128514, 2022.

585   Kusaka, H., Kondo, H., and Kikegawa, Y.: A simple single-layer urban canopy model for amtospheric models:
586   Comparison with multi-layer and slab models, Boundary-Layer Meteorology, 2001, 101., 101, 329–358, 2001.

587   Li, D., Malyshev, S., and Shevliakova, E.: Exploring historical and future urban climate in the Earth System
588   Modeling framework: 2. Impact of urban land use over the Continental United States, Journal of Advances
589   in Modeling Earth Systems, 8, 936-953, 10.1002/2015ms000579, 2016a.

590   Li, D., Malyshev, S., and Shevliakova, E.: Exploring historical and future urban climate in the Earth System
591   Modeling framework: 1. Model development and evaluation, Journal of Advances in Modeling Earth Systems,
592   8, 917-935, 10.1002/2015ms000578, 2016b.

593   Li, X., Fan, W., Wang, L., Luo, M., Yao, R., Wang, S., and Wang, L.: Effect of urban expansion on atmospheric

594   humidity in Beijing-Tianjin-Hebei urban agglomeration, Science of the total environment, 759, 144305,
595   10.1016/j.scitotenv.2020.144305, 2021.

596 Liang, S., Cheng, C., Jia, K., Jiang, B., Liu, Q., Xiao, Z., Yao, Y., Yuan, W., Zhang, X., Zhao, X., and Zhou, J.: The
597   Global LAnd Surface Satellite (GLASS) products suite, Bulletin of the American Meteorological Society,
598   102, E323-E337, 10.1175/BAMS-D-18-0341.1, 2021.

599 Liang, X. and Xie, Z.: A new surface runoff parameterization with subgrid-scale soil heterogeneity for land surface
600   models., Advances in Water Resources, 24, 1173-1193, 10.1016/S0309-1708(01)00032-X, 2001.

601 Liang, X., Wood, E. F., and Lettenmaier, D. P.: Surface soil moisture parameterization of the VIC-2L model:
602   evaluation and modification., Global and Planetary Change, 13, 195-206, 10.1016/0921-8181(95)00046-1,
603   1996.

604 Liang, X., Lettenmaier, D. P., Wood, E. F., and Burges, S. J.: A simple hydrologically based model of land surface
605   water and energy fluxes for general circulation models, Journal of Geographical Research, 99, 14415-14428,
606   10.1029/94JD00483 1994.

607 Liu, B., Xie, Z., Liu, S., Zeng, Y., Li, R., Wang, L., Wang, Y., Jia, B., Qin, P., Chen, S., Xie, J., and Shi, C.: Optimal
608   water use strategies for mitigating high urban temperatures, Hydrology and Earth System Sciences, 25, 387-
609   400, 10.5194/hess-25-387-2021, 2021.

610 Liu, J., Zhang, Z., Xu, X., Kuang, W., Zhou, W., Zhang, S., Li, R., Yan, C., Yu, D., and Wu, S.: Spatial patterns
611   and driving forces of land use change in China during the early 21st century, Journal of Geographical Sciences,
612   20, 483-494, 10.1007/s11442-010-0483-4, 2010.

613 Liu, Q., Zhang, S., Zhang, H., Bai, Y., and Zhang, J.: Monitoring drought using composite drought indices based
614   on remote sensing, Science of the total environment, 711, 134585, 10.1016/j.scitotenv.2019.134585, 2020a.

615 Liu, X., Zhou, Y., Yue, W., Li, X., Liu, Y., and Lu, D.: Spatiotemporal patterns of summer urban heat island in
616   Beijing, China using an improved land surface temperature, Journal of Cleaner Production, 257, 120529,
617   10.1016/j.jclepro.2020.120529, 2020b.

618 McNorton, J. R., Arduini, G., Bousserez, N., Agustí-Panareda, A., Balsamo, G., Boussetta, S., Choulga, M.,
619   Hadade, I., and Hogan, R. J.: An Urban Scheme for the ECMWF Integrated Forecasting System: Single-
620   Column and Global Offline Application, Journal of Advances in Modeling Earth Systems, 13,
621   10.1029/2020ms002375, 2021.

622 Meili, N., Paschalis, A., Manoli, G., and Fatichi, S.: Diurnal and seasonal patterns of global urban dry islands,
623   Environmental Research Letters, 17, 054044, 10.1088/1748-9326/ac68f8, 2022.

624 Meili, N., Manoli, G., Burlando, P., Bou-Zeid, E., Chow, W. T. L., Coutts, A. M., Daly, E., Nice, K. A., Roth, M.,
625   Tapper, N. J., Velasco, E., Vivoni, E. R., and Fatichi, S.: An urban ecohydrological model to quantify the
626   effect of vegetation on urban climate and hydrology (UT&C v1.0), Geoscientific Model Development, 13,
627   335-362, 10.5194/gmd-13-335-2020, 2020.

628 Meng, C.: The integrated urban land model, Journal of Advances in Modeling Earth Systems, 7, 759-773,
629   10.1002/2015ms000450, 2015.

630 Meng, F., Su, F., Li, Y., and Tong, K.: Changes in Terrestrial Water Storage During 2003–2014 and Possible Causes
631   in Tibetan Plateau, Journal of Geophysical Research: Atmospheres, 124, 2909-2931, 10.1029/2018jd029552,
632   2019.

633 Meng, S., Xie, X., Zhu, B., and Wang, Y.: The relative contribution of vegetation greening to the hydrological
634   cycle in the Three-North region of China: A modelling analysis, Journal of Hydrology, 591, 125689,
635   10.1016/j.jhydrol.2020.125689, 2020.

636 Mishra, V., Cherkauer, K. A., Niyogi, D., Lei, M., Pijanowski, B. C., Ray, D. K., Bowling, L. C., and Yang, G.: A
637   regional scale assessment of land use/land cover and climatic changes on water and energy cycle in the upper
638   Midwest United States, International Journal of Climatology, 30, 2025-2044, 2010.

639   Morabito, M., Crisci, A., Guerri, G., Messeri, A., Congedo, L., and Munafo, M.: Surface urban heat islands in
640   Italian metropolitan cities: Tree cover and impervious surface influences, Science of the total environment,
641   751, 142334, 10.1016/j.scitotenv.2020.142334, 2021.
642   Mu, X., Wang, H., Zhao, Y., Liu, H., He, G., and Li, J.: Streamflow into Beijing and Its Response to Climate
643   Change and Human Activities over the Period 1956–2016, Water, 12, 622, 10.3390/w12030622, 2020.
644   Nijssen, B., Schnur, R., and P. Lettenmaier, D.: Global retrospective estimation of soil moisture using the variable
645   infiltration capacity land surface model, 1980-93, Journal of Climate, 14, 1790-1808, 10.1175/1520-
646   0442(2001)014<1790:GREOSM>2.0.CO;2, 2001.
647   Oh, S.-G. and Sushama, L.: Urban-climate interactions during summer over eastern North America, Climate
648   Dynamics, 57, 3015-3028, 10.1007/s00382-021-05852-3, 2021.
649   Oleson, K. W. and Feddema, J.: Parameterization and Surface Data Improvements and New Capabilities for the
650   Community Land Model Urban (CLMU), J Adv Model Earth Syst, 12, e2018MS001586,
651   10.1029/2018MS001586, 2020.
652   Rodell, M., Houser, P. R., Jambor, U., Gottschalck, J., Mitchell, K., Meng, C.-J., Arsenault, K., Cosgrove, B.,
653   Radakovich, J., Bosilovich, M., Entin, J. K., Walker, J. P., Lohmann, D., and Toll, D.: The Global Land Data
654   Assimilation System, Bull. Amer. Meteor. Soc., 85, 381-394, https://doi.org/10.1175/BAMS-85-3-381, 2004.
655   Salvadore, E., Bronders, J., and Batelaan, O.: Hydrological modelling of urbanized catchments: A review and
656   future directions, Journal of Hydrology, 529, 62-81, 10.1016/j.jhydrol.2015.06.028, 2015.
657   Shangguan, W., Dai, Y., Liu, B., Zhu, A., Duan, Q., Wu, L., Ji, D., Ye, A., Yuan, H., Zhang, Q., Chen, D., Chen,
658   M., Chu, J., Dou, Y., Guo, J., Li, H., Li, J., Liang, L., Liang, X., Liu, H., Liu, S., Miao, C., and Zhang, Y.: A
659   China data set of soil properties for land surface modeling, Journal of Advances in Modeling Earth Systems,
660   5, 212-224, 10.1002/jame.20026, 2013.
661   Simón-Moral, A., Dipankar, A., Roth, M., Sánchez, C., Velasco, E., and Huang, X. Y.: Application of MORUSES
662   single-layer urban canopy model in a tropical city: Results from Singapore, Quarterly Journal of the Royal
663   Meteorological Society, 146, 576-597, 10.1002/qj.3694, 2019.
664   Sun, T. and Grimmond, S.: A Python-enhanced urban land surface model SuPy (SUEWS in Python, v2019.2):
665   development, deployment and demonstration, Geoscientific Model Development, 12, 2781-2795,
666   10.5194/gmd-12-2781-2019, 2019.
667   Wang, C., Wang, Z. H., and Yang, J.: Cooling Effect of Urban Trees on the Built Environment of Contiguous
668   United States, Earth's Future, 6, 1066-1081, 10.1029/2018ef000891, 2018.
669   Wang, Y., Xie, X., Liang, S., Zhu, B., Yao, Y., Meng, S., and Lu, C.: Quantifying the response of potential flooding
670   risk to urban growth in Beijing, Science of the total environment, 705, 135868,
671   10.1016/j.scitotenv.2019.135868, 2020.
672   Wang, Y., Xie, X., Shi, J., Zhu, B., Jiang, F., Chen, Y., and Liu, Y.: Accelerated hydrological cycle on the Tibetan
673   Plateau evidenced by ensemble modeling of Long-term water budgets, Journal of Hydrology, 615, 128710,
674   10.1016/j.jhydrol.2022.128710, 2022.
675   Xie, X., Liang, S., Yao, Y., Jia, K., Meng, S., and Li, J.: Detection and attribution of changes in hydrological cycle
676   over the Three-North region of China: Climate change versus afforestation effect, Agricultural and Forest
677   Meteorology, 203, 74-87, 10.1016/j.agrformet.2015.01.003, 2015.
678   Yang, G., Bowling, L. C., Cherkauer, K. A., Pijanowski, B. C., and Niyogi, D.: Hydroclimatic Response of
679   Watersheds to Urban Intensity: An Observational and Modeling-Based Analysis for the White River Basin,
680   Indiana, Journal of Hydrometeorology, 11, 122-138, 10.1175/2009jhm1143.1, 2010.
681   Yang, L., Ni, G., Tian, F., and Niyogi, D.: Urbanization Exacerbated Rainfall Over European Suburbs Under a
682   Warming Climate, Geophysical Research Letters, 48, 10.1029/2021gl095987, 2021.
683   Yao, R., Wang, L., Huang, X., Liu, Y., Niu, Z., Wang, S., and Wang, L.: Long-term trends of surface and canopy

684   layer urban heat island intensity in 272 cities in the mainland of China, Science of the total environment, 772,
685   145607, 10.1016/j.scitotenv.2021.145607, 2021.

686 Zhang, X., Zhao, X., Li, W., Liang, S., Wang, D., Liu, Q., Yao, Y., Jia, K., He, T., Jiang, B., Wei, Y., and Ma, H.:
687   An Operational Approach for Generating the Global Land Surface Downward Shortwave Radiation Product
688   From MODIS Data, IEEE Transactions on Geoscience and Remote Sensing, 57, 4636-4650,
689   10.1109/tgrs.2019.2891945, 2019.

690 Zhao, Q., Ding, Y., Wang, J., Gao, H., Zhang, S., Zhao, C., Xu, J., Han, H., and Shangguan, D.: Projecting climate
691   change impacts on hydrological processes on the Tibetan Plateau with model calibration against the glacier
692   inventory data and observed streamflow, Journal of Hydrology, 573, 60-81, 10.1016/j.jhydrol.2019.03.043,
693   2019.

694 Zhong, X., Wang, L., Zhou, J., Li, X., Qi, J., Song, L., and Wang, Y.: Precipitation Dominates Long-Term Water
695   Storage Changes in Nam Co Lake (Tibetan Plateau) Accompanied by Intensified Cryosphere Melts Revealed
696   by a Basin-Wide Hydrological Modelling, Remote Sensing, 12, 1926, 10.3390/rs12121926, 2020.

697 Zhou, D., Xiao, J., Bonafoni, S., Berger, C., Deilami, K., Zhou, Y., Frolking, S., Yao, R., Qiao, Z., and Sobrino, J.:
698   Satellite Remote Sensing of Surface Urban Heat Islands: Progress, Challenges, and Perspectives, Remote
699   Sensing, 11, 48, 10.3390/rs11010048, 2018.

700 Zhou, J., Li, J., and Yue, J.: Analysis of urban heat island (UHI) in the Beijing, IGARSS, 3327-3330, 2010.

701 Zhu, B., Xie, X., Meng, S., Lu, C., and Yao, Y.: Sensitivity of soil moisture to precipitation and temperature over
702   China: Present state and future projection, Science of The Total Environment, 705, 135774,
703   https://doi.org/10.1016/j.scitotenv.2019.135774, 2020.

704 Zhu, B., Xie, X., Lu, C., Lei, T., Wang, Y., Jia, K., and Yao, Y.: Extensive Evaluation of a Continental-Scale High-
705   Resolution Hydrological Model Using Remote Sensing and Ground-Based Observations, Remote Sensing,
706   13, 1247, 10.3390/rs13071247, 2021.

707